

Atlantic Water Boundary Current Along the Southern Yermak Plateau, Arctic Ocean

**Key Points:**

- The Atlantic Water boundary current transport along the southern Yermak Plateau is maximum (1.4 Sv) in fall and minimum (0.8 Sv) in summer
- Surface water divergence along the northwest Spitsbergen coast regulates the volume transport between the Svalbard and Yermak branches
- A previously undocumented cold, bottom-intensified deep current is observed in all seasons

Correspondence to:

I. Fer,
ilker.fer@uib.no

Citation:

Fer, I., Peterson, A. K., & Nilsen, F. (2023). Atlantic water boundary current along the southern Yermak Plateau, Arctic Ocean. *Journal of Geophysical Research: Oceans*, 128, e2023JC019645. <https://doi.org/10.1029/2023JC019645>




Received 10 JAN 2023
Accepted 15 MAY 2023

Author Contributions:

Conceptualization: Ilker Fer
Data curation: Ilker Fer, Algot K. Peterson, Frank Nilsen
Formal analysis: Ilker Fer, Frank Nilsen
Funding acquisition: Ilker Fer
Investigation: Ilker Fer, Algot K. Peterson
Methodology: Ilker Fer
Project Administration: Ilker Fer
Resources: Ilker Fer
Software: Ilker Fer, Algot K. Peterson
Supervision: Ilker Fer
Validation: Ilker Fer
Visualization: Ilker Fer, Algot K. Peterson, Frank Nilsen
Writing – original draft: Ilker Fer, Frank Nilsen
Writing – review & editing: Ilker Fer, Algot K. Peterson, Frank Nilsen

© 2023. The Authors.

This is an open access article under the terms of the [Creative Commons Attribution License](#), which permits use, distribution and reproduction in any medium, provided the original work is properly cited.

Ilker Fer^{1,2} , Algot K. Peterson^{1,3} , and Frank Nilsen^{1,2} 

¹Geophysical Institute, University of Bergen, Bergen, Norway, ²The University Centre in Svalbard (UNIS), Longyearbyen, Norway, ³Now at Multiconsult Norge AS, Bergen, Norway

Abstract The major ocean current that carries heat into the Arctic Ocean splits into three main branches of Atlantic Water (AW) and recirculations when it encounters the Yermak Plateau (YP) located north of Svalbard. While the branches that cross the plateau and recirculations have been extensively studied, there has been limited observation of the transport and variability of the Yermak branch. In this study, we present year-round observations from an array of three moorings that were deployed across the boundary current on the southern slope of the YP. The temporal-averaged sections show a surface-intensified AW core, which is strongest in winter but also persistent throughout the record within the upper 500 m. The volume transport of AW is highest in fall (1.4 ± 0.2 Sv; $1 \text{ Sv} = 10^6 \text{ m}^3 \text{ s}^{-1}$) and decreases to 0.8 ± 0.1 Sv in summer. Beneath a surface-intensified core, the velocity profile has a minimum at middepth, gradually increasing toward the bottom. This cold, bottom-intensified current is detectable in all seasons and reaches a maximum transport of 1.5 Sv in spring. The transport of AW is regulated by wind stress curl and coastal upwelling along the northwestern shelf of Svalbard. A positive wind stress curl increases the volume transport in the Yermak branch, thereby reducing the Svalbard branch transport. Eddy kinetic energy is surface-intensified and decreases to negligible values below 500 m. In the upper 500 m, the average baroclinic conversion in winter and summer is about $1 \times 10^{-5} \text{ W m}^{-3}$, which is 4–10 times the barotropic conversion rates.

Plain Language Summary We conducted year-long measurements of temperature, salinity, and ocean currents using an array of instruments in the southern part of Yermak Plateau, located northwest of Svalbard. The array covers the ocean current that carries warm Atlantic Water—an important contributor of heat to the Arctic Ocean. Using the observations, we describe the structure and seasonal changes of the currents and how much water they transport into the Arctic. This is the first study to collect year-round data on this part of the ocean. We found that the amount of warm water transported varied by season and was highest in the fall. Wind patterns also influenced how the warm water flow was divided between different pathways. We also discovered a previously unknown deep current of cold water flowing in the same direction as the warm water current. This cold water flow was persistent in all seasons and transported similar amounts of water as the warm water flow.

1. Introduction

The poleward flow of Atlantic-origin water is the primary contributor of oceanic salt and heat to the Arctic Ocean, with significant effects on the thermohaline structure, sea ice distribution and marine ecosystems in the Arctic system (Dörr et al., 2021; Ingvaldsen et al., 2021; Polyakov et al., 2017). One of the major branches of this warm and saline AW supply is the West Spitsbergen Current (WSC), which is the northward extension of the Norwegian Atlantic Current along the west coast of Svalbard in Fram Strait (Figure 1) (Aagaard et al., 1987; Beszczynska-Möller et al., 2012). Fram Strait, located between Greenland and Svalbard, serves as a deep connection between the Arctic Ocean and the Nordic Seas, facilitating the main exchange between the AW and the cold and fresh polar waters (Quadfasel et al., 1987; Schauer et al., 2004). In Fram Strait, the WSC carries the AW northward, whereas the East Greenland Current (EGC) carries the cold and fresh polar waters southward. Additionally, the Atlantic-origin water that recirculates in Fram Strait and circulates in the Arctic Ocean are exported out via the EGC.

The WSC has been monitored since 1997 by the Alfred Wegener Institute, Germany, with a mooring array along $78^\circ 50' \text{N}$ (Beszczynska-Möller et al., 2012; Schauer et al., 2004). At this latitude, the WSC consists of two branches: the Svalbard branch, which is confined to the 400–500 m isobaths (Aagaard et al., 1987), and

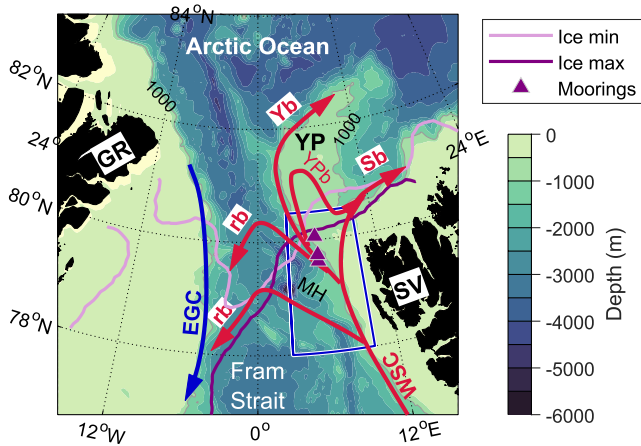


Figure 1. The map shows the study area in Fram Strait, located between Greenland (GR) and Svalbard (SV). The triangles mark the location of moorings on the southern part of Yermak Plateau. The region shown in Figure 2 is outlined. The red arrows illustrate the branches of the Atlantic Water current (WSC, West Spitsbergen Current; Sb, Svalbard branch; Yb, Yermak branch; YPb, Yermak Pass branch; rb, recirculating branch), while the blue arrow represents the East Greenland Current. Molloy Hole is also marked. The isobaths are from the two arc-minute resolution ETOPO Global Relief Model (NOAA National Geophysical Data Center, 2006), and the 1,000 m contour is highlighted. The light and dark purple lines show the minimum and maximum extent of sea ice during the mooring observation period.

an outer branch that spans between the 1,000 m and 1,500 m isobaths (referred to as the WSC core and the WSC offshore branch, respectively, by Beszczynska-Möller et al. (2012)). The Svalbard branch originates directly from the Norwegian Atlantic Slope Current, and is topographically steered and barotropic, influenced by the sea surface slope variability. In contrast, the offshore branch exhibits a stronger vertical shear and originates from the baroclinic Norwegian Atlantic Front Current that flows along the Mohn and Knipovich ridges before merging with the Svalbard branch (Orvik & Niiler, 2002; Walczowski et al., 2005). The northward volume transport of AW warmer than 2°C across the 78°50'N mooring array, averaged over 1997–2010, is 3.0 ± 0.2 Sv (1 Sv $\equiv 10^6$ m³ s⁻¹), with 1.3 ± 0.1 Sv carried in the Svalbard branch (Beszczynska-Möller et al., 2012). The AW inflow shows strong seasonality, with the lowest inflow observed in summer and approximately doubling in late autumn/winter. It is estimated that 50%–80% of the total northward flowing AW recirculates and flows south, joining the EGC (Bourke et al., 1988; Manley, 1995; Quadfasel et al., 1987). Multi-year mooring-based observations at the prime meridian showed a continuous westward flow of the AW at 78°50'N, present throughout the year and most affected by eddies in spring (Hofmann et al., 2021).

Moving further north, the topographic fracture zones and diverging isobaths of the YP play a crucial role in shaping the circulation pattern of the AW (Figure 1). A fraction of the outer branch of the WSC recirculates north of the Molloy Hole (MH), while another portion follows the 1,000–1,500 m isobaths (Manley, 1995) along the rim of the YP (known as the Yermak branch). At 80°10'N, mooring data spanning two years show, in contrast to the continuous westward flow at 78°50'N, that the recirculation takes place

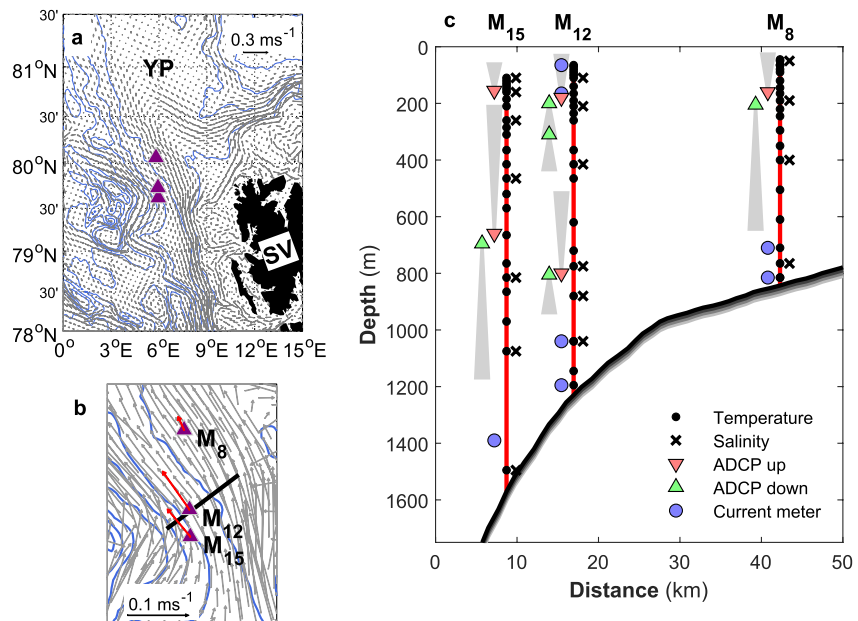


Figure 2. Overview of the mooring array and time-averaged currents. (a) Map of the mooring locations (triangles) and water depth contours (blue, ETOPO-2) at intervals of 500 m, overlaid with 6-year (2005–2010) time and depth-averaged current vectors drawn for every eighth grid point (for visibility) from the 800-m resolution model fields (Hattermann et al., 2016). A scale is provided in the upper right corner. (b) A close-up view of panel (a) near the mooring site showing the observed time and depth-averaged current vectors (red arrows) at moorings M_8 , M_{12} , and M_{15} . (c) A section across the isobaths along the black line marked in (b) showing the coverage and sensor distribution of the moorings. M_{15} is located 10 km upstream of the target section and M_8 is located 30 km downstream.

Table 1
Details of Mooring Deployment and Recovery

Mooring	M ₈	M ₁₂	M ₁₅
Longitude	5°E 48.733'	5°E 56.333'	5°E 57.541'
Latitude	80°N 03.876'	79°N 44.093'	79°N 37.209'
Water depth (m)	840	1,225	1,560
Deployed (UTC)	10.09.2014 09:05	11.09.2014 10:47	10.09.2014 18:55
Recovered (UTC)	13.08.2015 08:00	13.08.2015 13:00	13.08.2015 17:00

Note. Total depth is estimated using the deepest pressure gauge, mooring line setup, and the ship's echo sounder. Mooring names correspond to the approximate isobath in 100 m where the mooring was deployed. The names used in the data report (Peterson & Fer, 2017) are Y2 (M₈), Y3 (M₁₂), and Y1 (M₁₅).

in the form of passing eddies, which are most intense during late autumn and winter, and absent during summer (Hofmann et al., 2021). In line with these observations, a high-resolution model shows that the northern recirculation fraction of the warmest AW occurs mainly due to eddies north of 80°N (Hattermann et al., 2016). The model also reveals a seasonal variability in the northern recirculation fraction, which roughly doubles in winter and spring, likely due to increased eddy activity during those seasons. The increase in eddy energy is related to enhanced storm activity in winter and a baroclinically unstable WSC in winter months (von Appen et al., 2016).

An ocean observing program conducted over a period of two years (2014–2016) using altimetry and re-analysis wind data revealed that the variability of the Svalbard branch on the YP is controlled by upstream wind stress curl along the West Spitsbergen Shelf, with a peak-to-peak variability that exceeds 4 Sv (Nilsen et al., 2021). In addition to the Svalbard and Yermak branches and the recirculations, a shortcut across the plateau was discovered through the use of acoustically tracked subsurface floats, which was named the Yermak Pass branch (Gascard et al., 1995). Current measurements at a depth of 745 m were reported by Koenig et al. (2017) in the Yermak Pass during a yearlong study in 2007, with continuous ocean current measurements available only between depth ranges of 500–570 m and 250–380 m and no temperature or salinity records. The currents exhibited a variability at a time scale of 5–15 days during winter, which was proposed to be related to the Yermak Pass branch. This branch was also detected in model outputs (with a resolution of 4–5 km) primarily during winter (Koenig et al., 2017). Ten years later, a 36-month mooring record collected between 2017 and 2020 confirmed the presence of the Yermak Pass branch and also showed its intensification during periods of reduced sea ice concentrations (SICs) (Artana et al., 2022).

The above literature review highlights the lack of year-round measurements of the Yermak branch. The structure and variability of currents, volume transports, and hydrography are not well-constrained. This paper aims to fill this gap by presenting observations from an array of three moorings on the southern YP, covering the AW boundary current along the slope. The target location for the mooring array, aimed to capture the Yermak branch across 81°N, was inaccessible due to challenging sea-ice conditions. While the deployed location (Figure 1) is not ideal and includes potential contributions to the Yermak Pass the recirculation branches, we use the observations to estimate the volume transport in temperature classes and quantify the contribution of the Yermak branch. Using the new observations, we document the structure and seasonal variation of the Yermak branch, mesoscale current variability, and energy conversion rates. Furthermore, we examine the role of barotropic and baroclinic instabilities in the variability of the Yermak branch. Finally, we describe how the wind stress curl along the Svalbard branch pathway regulates the volume transport of the Yermak branch.

2. Data

2.1. Moorings

The velocity, temperature and salinity were measured using instruments attached to an array of three moorings that were deployed on the southwestern slope of the YP, northwest of Svalbard, from 10 September 2014 to 13 August 2015 (Figures 1 and 2). The moorings are named M₈, M₁₂, and M₁₅ with the figures corresponding to the approximate landing isobath of the mooring in 100 m (e.g., M₁₂ is at 1,200 m). Mooring locations and deployment and recovery details are given in Table 1.

The moorings were densely instrumented, and sampled at hourly rate or faster, covering a large fraction of the water column. See Table 2 and Figure 2c for details of the instrument distribution on moorings. Currents were

Table 2
Mooring Instrument Details

Mooring	Instrument depth (m)	Parameter	Instrument
M₈	65, 80, 90, 120, 145, 164, 220, 245, 295, 350, 610, 710, 815	<i>T</i>	SBE56
	505	<i>T, P</i>	SBE39
	45*, 190*, 400, 765*	<i>C, T, P*</i>	SBE37
	165 ^U	<i>U, W, P</i>	RDI 150 kHz
	167 ^D	<i>U, W, P</i>	RDI 75 kHz
	710, 815*	<i>T, C, U, P*</i>	RCM7
M₁₂	70, 80, 90, 100, 140, 190, 235, 260, 365, 465, 620, 720, 1,145	<i>T</i>	SBE56
	110*, 210*, 415, 775, 880*, 1,041*	<i>C, T, P*</i>	SBE37
	184 ^U , 830 ^U	<i>U, W, P</i>	RDI 150 kHz
	186 ^D , 306 ^D , 832 ^D	<i>U, W, P</i>	RDI 300 kHz
	65*, 165*, 1,195	<i>C, T, P, U, O*</i>	SeaGuard
	1,040	<i>U, T</i>	RCM7
M₁₅	120, 130, 140, 150, 185, 210, 285, 310, 415, 520, 665, 765, 865, 970	<i>T</i>	SBE56
	365, 570	<i>T, P</i>	SBE39
	110*, 161*, 260*, 465, 815*, 1,075, 1,495*	<i>C, T, P*</i>	SBE37
	160 ^U	<i>U, W</i>	RDI 300 kHz
	668 ^U , 672 ^D	<i>U, W, P</i>	RDI 75 kHz
	1,390	<i>T, C, U</i>	RCM7

Note. The instrument depth is the corrected average depth based on the mooring line length and pressure record obtained from the instruments. The parameters are temperature (*T*), conductivity (*C*), pressure (*P*), horizontal velocity (*U*), vertical velocity (*W*), and dissolved oxygen (*O*). In this study, *W* and *O* are not used. Instruments are identified by their type (see text), and a superscript U/D indicates upward/downward pointing ADCPs, respectively. Parameters marked by an asterisk (*) are only sampled by the instruments at the marked depths (e.g., SBE37 at 400 m at M₈ did not sample pressure).

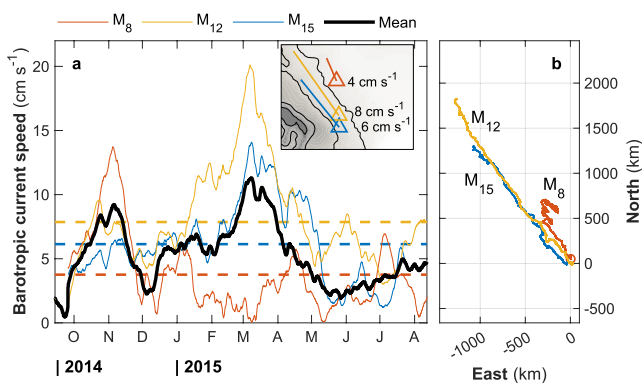


Figure 3. Barotropic currents at the moorings were approximated by vector averaging the horizontal velocity components over a depth range of 100 m below the surface to 100 m above the seabed. (a) Time series of the depth-averaged current speed filtered using a monthly moving average. The black curve represents the average current speed obtained from the three moorings, while the horizontal dashed lines indicate the modulus of the time-averaged velocity at each mooring. The inset shows the time-averaged vectors at each mooring overlaid on the bathymetric contours (ETOPO2). (b) Progressive vector diagrams created using hourly depth-averaged currents (not filtered) originating from each mooring position.

measured using acoustic Doppler current profilers (ADCPs, RDI 75 kHz, 150 and 300 kHz Workhorses) and current meters (Aanderaa SeaGuard or Recording Current Meter, RCM7). Most current profilers and current meters also measured the pressure. Temperature, salinity and pressure were sampled using Sea-Bird Scientific (SBE) conductivity-temperature-depth recorders (CTD, SBE37 Microcats), and temperature loggers (SBE56 and SBE39). Further details can be found in the data report (Peterson & Fer, 2017), where the original mooring names are Y2 (M₈), Y3 (M₁₂), and Y1 (M₁₅). Not shown in Table 2 and Figure 2c are three SBE39s (one on each mooring) with temperature and pressure sensors, and a deep (50 m above seabed) RCM7 at M₁₅, which did not record any data. Although conductivity sensors are listed for RCM7s, their quality is not good and are not used to derive salinity and not shown in Figure 2c. The Microcats at M₈ depleted their batteries in late May 2015, and salinity measurements are not available in summer 2015 for this mooring. The temperature loggers, ADCPs and current meters at M₈ collected data throughout the deployment duration. Because of the relatively coarse coverage of salinity measurements, we use temperature and Practical Salinity (salinity hereafter), instead of the Conservative Temperature and Absolute Salinity. The initial accuracy of the SBE sensors are $\pm 2 \times 10^{-3}^{\circ}\text{C}$ for temperature, $\pm 3 \times 10^{-4} \text{ S m}^{-1}$ for conductivity, and ± 1 dbar for pressure. Velocity measurements are accurate to better than 1 cm s^{-1} in speed and $\pm 2^{\circ}$ in direction. Conservative error estimates are $\pm 0.01^{\circ}\text{C}$ for temperature, ± 0.01 for salinity, and $\pm 1 \text{ cm s}^{-1}$ for velocity (but large, $O(10^{\circ})$ direction errors can be expected for some ADCPs, see below).

The data from each mooring were used to create a gridded data set, which was corrected for mooring motion (blow down). Instruments that sampled faster than the hourly rate were bin-averaged and linearly interpolated to the common grid of 1 hr temporal and 5 m vertical resolution. Occasional blow down of the mooring lines due to strong currents was corrected for by interpolating the pressure records. Before creating the gridded data set, each sensor was quality controlled and checked for consistency against nearby instruments and shipboard CTD profiles obtained before mooring recovery. When necessary, small constant offset corrections were made to conductivity and temperature records to ensure a smooth time-averaged profile. The data excluded occasional long-term blocking of unpumped conductivity cells. The compass of four ADCPs was unusable due to their erroneous deployment in an orientation that was opposite to their calibration. For these instruments, the currents were rotated to align with the nearest overlapping current measurements from an independent instrument or by matching the direction of currents in the nearest bins of upward and downward pointing ADCP pairs on the same buoy. The mooring data are available from Fer and Peterson (2019), and further details can be found in the data report (Peterson & Fer, 2017).

Despite the efforts made from the ice-class coast guard vessel *Svalbard*, unfavorable sea ice conditions during the cruise prevented accessing the target site near 81°N, forcing the mooring array to be relocated to the south at 80°N. Furthermore, the moorings could not be deployed along a line normal to the isobath orientation (Figure 2). As a result, we focus on a section extracted across the M_{12} location, which is used to generate daily fields, sections, and transport calculations (Sections 3 and 4). The along-isobath distance from M_8 and M_{15} to the section is approximately 30 and 10 km, respectively, along which the flow can be assumed coherent. This assumption is supported by the 800-m resolution model, which shows that the daily averaged along-isobath currents at our study site are coherent at these length scales. However, the horizontal separation from the target section, which is greater than the internal Rossby radius of deformation (5–10 km), may have implications for mesoscale statistics, as discussed in Section 3.3.

The coordinate system is rotated with 125° from East, with x and y directed positive along-isobath and off-slope toward deeper water, with along-isobath, u and across-isobath, v , velocity components.

2.2. Supporting Data

We extracted wind speed and direction at 10 m above sea level at hourly intervals in the area north of Svalbard (0°–30°E, 76°–83°N) from the Norwegian Reanalysis Archive (NORA10; Reistad et al. (2011)). NORA10 is a regional high-resolution (10–11 km) atmospheric downscaling of ERA-40 (Uppala et al., 2005) and ECMWF IFS (European Center for Medium-Range Weather Forecasts Integrated Forecasting System) operational analyses (after 2002) that covers the northern North Atlantic and the Barents Sea. The dynamic atmospheric downscaling is performed as a series of short prognostic runs (using High Resolution Limited Area Model) initialized from a blend of ERA-40 and the previous prognostic run. This preserves the fine-scale surface features from the high-resolution model while maintaining the large-scale synoptic field from ERA-40. We calculated the wind stress components using the Large and Pond (1981) parameterization and the wind stress curl over the region of interest north of Svalbard. We also extracted hourly time series from NORA10 at the grid point closest to the M_{12} mooring location.

We acquired SIC data from EUMETSAT Ocean and Sea Ice SAF (OSI-SAF, 2017). The data grid has an approximate resolution of 10 km, and we interpolated the data linearly to the mooring locations. We defined the ice edge as the boundary where the SIC reaches 10%. The distance to the ice edge was calculated as the shortest distance to this boundary.

3. Observations

3.1. Low-Frequency Variability

The moorings were positioned in the Yermak branch, and M_{12} is located at the core of the AW current (Figure 2). The circulation pattern in the study region can be seen from the 5-year average of depth-averaged currents from the regional model output (Hattermann et al., 2016) shown in Figure 2. The barotropic currents from the moorings were approximated by vector-averaging the horizontal velocity components over the depth range of 100 m below surface to 100 m above the seabed. The depth-averaged currents observed over the deployment duration were directed toward the northwest along the isobaths, in agreement with the model fields. The average value of

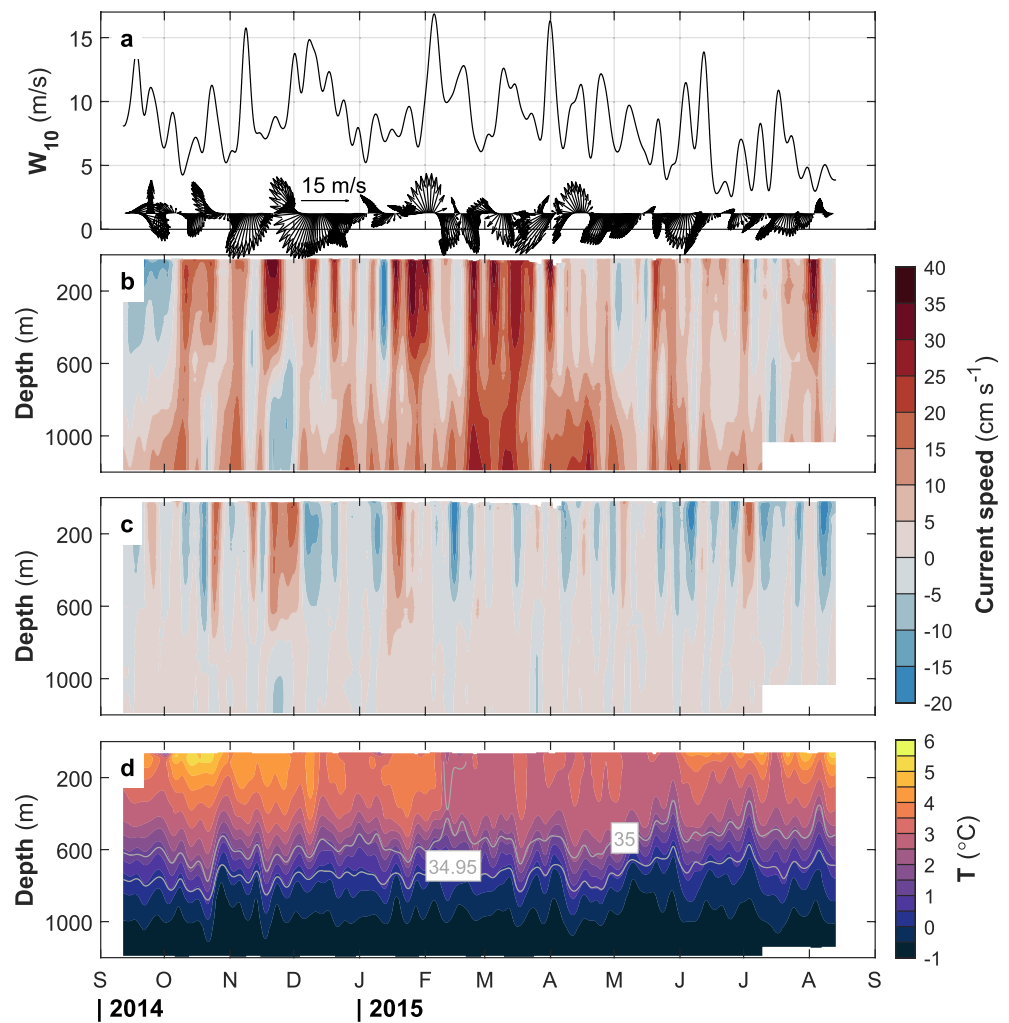


Figure 4. Overview of the wind forcing and observations at M_{12} . All data shown have been consistently low-pass filtered using a 7-day cutoff. (a) The hourly wind speed at 10-m height and wind velocity vectors (shown every 12 hr for clarity) from NORA-10 at the grid point near the mooring location. Depth–time distribution of (b) along-isobath velocity, u , (c) across-isobath velocity, v , and (d) temperature, T . Gray contours are for Practical Salinity values of 35 and 34.95.

the depth-averaged current at M_{12} was 8 cm s^{-1} . However, the depth-averaged currents were highly variable, with the strongest currents observed in November and March (Figure 3). In March, when the strongest currents were observed at M_{12} , the currents at M_8 were the weakest, indicating substantial lateral shear. The progressive vector diagrams, using hourly depth-averaged currents, show a clear along-isobath advection at the two deeper moorings, whereas M_8 was characterized by looping and eddying horizontal displacements in the latter half of the record.

The time series of depth-averaged currents can be compared to the wind forcing presented in Figure 4, which also shows the depth-time distribution of low-passed along-isobath and across-isobath velocity components and temperature at M_{12} . The along-isobath current frequently reaches 40 cm s^{-1} , and particularly in March, it is strong throughout the water column. There is strong variability on a weekly time scale in both along-isobath and across-isobath components, with enhanced currents in the upper 600 m. Several events of alternating bands of positive and negative across-isobath currents are visible (in October, December, January, and July), suggesting recirculation. The upper half of the water column is characterized by relatively warm water ($>2^\circ\text{C}$), while bottom-enhanced along-isobath currents are associated with cold waters. Bottom-enhanced currents are a typical feature at M_{12} , and are apparent in time-averaged profiles in all seasons (see Figure 7 introduced later).

The sea ice cover can affect the boundary current structure and dynamics. When coupled with an initially surface-intensified, laterally sheared geostrophic current, sea ice can modify the vertical structure of the

geostrophic velocity, leading to a subsurface velocity core (Leng et al., 2022). Throughout the duration of our measurements, the ice concentration at the two deeper moorings was typically less than 10%, and the distance to ice edge varied between 0 and 100 km (Figure 5). Therefore, we do not expect the ice conditions during the measurement period to affect the vertical structure at the core. At the northernmost and shallow mooring location, the SIC frequently reached 40%.

3.2. Average Sections and Profiles

Keeping in mind the limitations of an array with only three moorings that are not arranged normal to the bathymetry, we construct depth–cross-isobath sections using the 1-hr and 5-m vertically gridded mooring data sets. First, we apply a low-pass filter to the records from each mooring using a 35-hr cutoff to remove tidal and other high-frequency variability. We then average the records over 24 hr. Next, we optimally interpolate daily averaged profiles from the three moorings onto a regular grid using a two-dimensional Gaussian covariance function: $\text{cov}(y, z) = e\delta(y, z) + (1 - e) \exp(-y^2/L_y^2 - z^2/L_z^2)$ with δ being the Dirac function, $e = 0.05$ the relative error (i.e., the uncorrelated noise is set to 5% of the signal strength), and correlation scales $L_y = 20$ km and $L_z = 100$ m. We use the resulting daily fields of velocity and temperature in transport calculations (Section 4). In this section, we present the seasonal and annual time-averaged structure (Figure 6). Annual average is the average over the full record length. Summer is defined as the months of June, July, and August (JJA), and winter as December, January, and February (DJF).

The section of the along-isobath current shows a surface-intensified AW core, which is strongest in winter (Figure 6c) but is also persistent year-round (Figure 6a) at M_{12} . Across the section, the waters above 500 m depth remain above 2°C in all seasons and in the annual average. Beneath the AW core, there is a strong undercurrent of cold waters in the same direction as the AW boundary current. This cold boundary current is particularly strong in winter and spring. Note that the structure associated with the cold water is not an artifact of the objective interpolation, as it is also apparent in the average profiles from M_{12} (Figure 7).

Time-averaged profiles of temperature and velocity components at the core mooring M_{12} show the mean structure in different seasons (Figure 7). The along-isobath component is consistently positive, with a relatively slow middepth current sandwiched between the surface-intensified AW core and the bottom-intensified cold current. There is also discernible across-isobath current variability in the AW relative to the deeper half of the water column. The highest upper layer temperatures are observed in the fall season. Below 100 m, the AW is about 0.3°C warmer in winter than in summer, likely due to vertical mixing of warm waters in fall. The average currents in winter are typically twice as strong as in summer and fall throughout the water column.

Moorings M_{15} and M_{12} , are separated by about 8 km and have CTD sensors between 100 and 1,100 m, which allow for an estimate of geostrophic velocity profiles. The geostrophic velocity profiles referenced to direct measurements at 600 m depth are shown in Figure 7b for the winter and summer profiles (other seasons are similar). The shape of the velocity profiles is consistent with the geostrophic shear.

3.3. Overview of Mesoscale and High-Frequency Variability

The time-averaged background structure presented above is influenced by the mesoscale ($O(1 - 10)$ day) and higher frequency variability dominated by tides such as the diurnal K_1 and semidiurnal M_2 constituents, and near-inertial currents. This is seen in the frequency spectra of along-isobath and across-isobath currents, which have been averaged over selected levels (Figure 8). It is known that diurnal tidal currents are intensified along the upper slope of the YP (Padman et al., 1992). The high-frequency variability is beyond the scope of this study. Peterson (2017) and Wang et al. (2022), have described the near-inertial and the tidal variability, respectively, using the data from the moorings used here. We identified the 35-hr to 14-day band-range of interest for analyzing the energetics associated with eddies and mesoscale variability from the spectrum.

To calculate fluctuations in the mesoscale, we applied a band-pass filter to the hourly data using cutoff frequencies corresponding to 14 days and 35 hr. Hovmöller plots of the band-passed velocity at two selected levels, one near the surface at 150 m and one close to the velocity minimum at 600 m, are shown in Figure 9. Across the mooring array, the outer two moorings show the most variability in both velocity components, although the energetic features are frequently observed at the shallow mooring at the 800-m isobath. At 150 m depth,

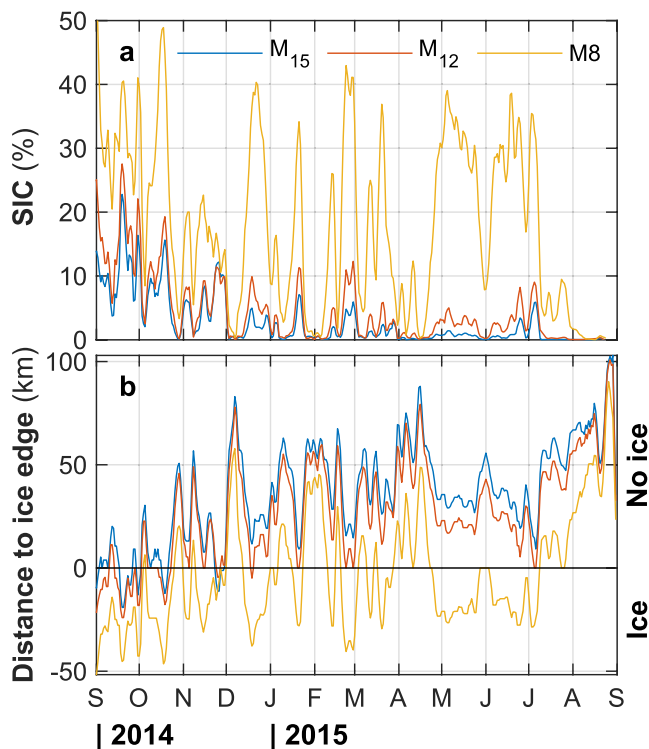


Figure 5. Ice conditions at the mooring locations. (a) Sea ice concentration (SIC), and (b) the distance to the sea-ice edge, which is defined as 10% concentration. The SIC data were obtained from EUMETSAT Ocean and Sea Ice SAF (OSI-SAF, 2017).

the largest mesoscale variability is observed during winter. At 600 m depth, the band-passed currents are substantially suppressed relative to 150 m, and the variability is mainly seen in winter and early spring, particularly in the records from the shallow mooring. The mesoscale variability and the energetics are presented in detail in Section 5.

We assume that the three moorings lie exactly on a line, despite the fact that M_8 and M_{15} are approximately 30 and 10 km away from the target section, respectively. For the shallowest mooring, with an average current of 4 cm s^{-1} , this corresponds to an advective time of 8.7 days (approximately 2 days at M_{15} , with 6 cm s^{-1}). Although we do not expect significant effects on our seasonal sections or our monthly and seasonal volume transport estimates, the horizontal separation from the target section may have consequences for the interpretation of mesoscale statistics. In the analysis of Figure 9, signals are not offset in the cross-isobath direction and may arrive at the shallowest mooring about 9 days later. Hofmann et al. (2021) observed unrelated statistics between moorings with a 75 km separation from their zonal mooring array in the recirculation region in the mid-Fram Strait. Their moorings are away from the continental slope, over irregular topography and affected by the proximity of MH, whereas our mooring array is on a slope where the boundary current is relatively well-defined and guided by topography. We would expect relatively coherent mesoscale statistics between our adjacent moorings. Our calculations for the conversion rates in Section 5 are based on the M_{12} mooring, with lateral gradients obtained between M_{15} and M_{12} , and therefore, the along-isobath distance to the target section has a negligible effect.

4. Transport

We use the daily fields of velocity and temperature, obtained from objective interpolation, to calculate the volume transport by integrating the along-isobath component of the current. A positive transport is northwestward (Q_p) toward the Arctic Ocean, while a negative transport is directed southeastward (Q_n). The total transport is also computed in increments of 1°C temperature classes. The AW transport (Q_{AW}) is estimated as the net transport of water warmer than or equal to 2°C , consistent with Beszczynska-Möller et al. (2012). The results are summarized in Figure 10 and Table 3.

Error estimates on the transport values are reported in the form of standard error and overall uncertainty. The standard error is calculated as σ/\sqrt{n} , where σ is the standard deviation of daily estimates over a given averaging period (seasons or annual). The effective degrees of freedom, n , is calculated by dividing the length of daily records by a decorrelation time scale of 7 days, which is estimated by integrating the auto-covariance sequence of transport over 100 days. The value of n varies between 10 and 13 for different seasons, and $n = 48$ for the annual analysis.

To estimate the total error on the transport values, we use the error map from objective interpolation and measurement errors. Daily fractional error maps of temperature and velocity are averaged over the analysis period (seasonal and annual separately; time variability of mapping error over the analysis period is negligible). These maps are converted into error fields in temperature and velocity units by multiplying them by the mapped temperature and velocity. We add a measurement uncertainty of 2 cm s^{-1} and 0.02°C at the mooring locations where we have measurements and zero mapping error. We then multiply each error field with random values drawn from the standard normal distribution and add to the temperature and velocity fields. This process is repeated 1,000 times, and each time the transport is calculated by integrating vertically and laterally. The total error is then obtained as the root-mean-square value over the 1,000 values of difference between the actual transports and the transport with errors. The total error estimates are typically 0.1 Sv in summer/spring and 0.2 Sv in winter/fall, which are less than the standard errors (see Table 3). We propose that the larger standard errors represent the variability over the averaging period, while the total error is a representative estimate of the average transport error.

Daily transport estimates show large variability with occasional flow reversals (Figure 10a). Typically, the total transport is northward, and the largest reversals occur during the winter months. Monthly averages of the AW

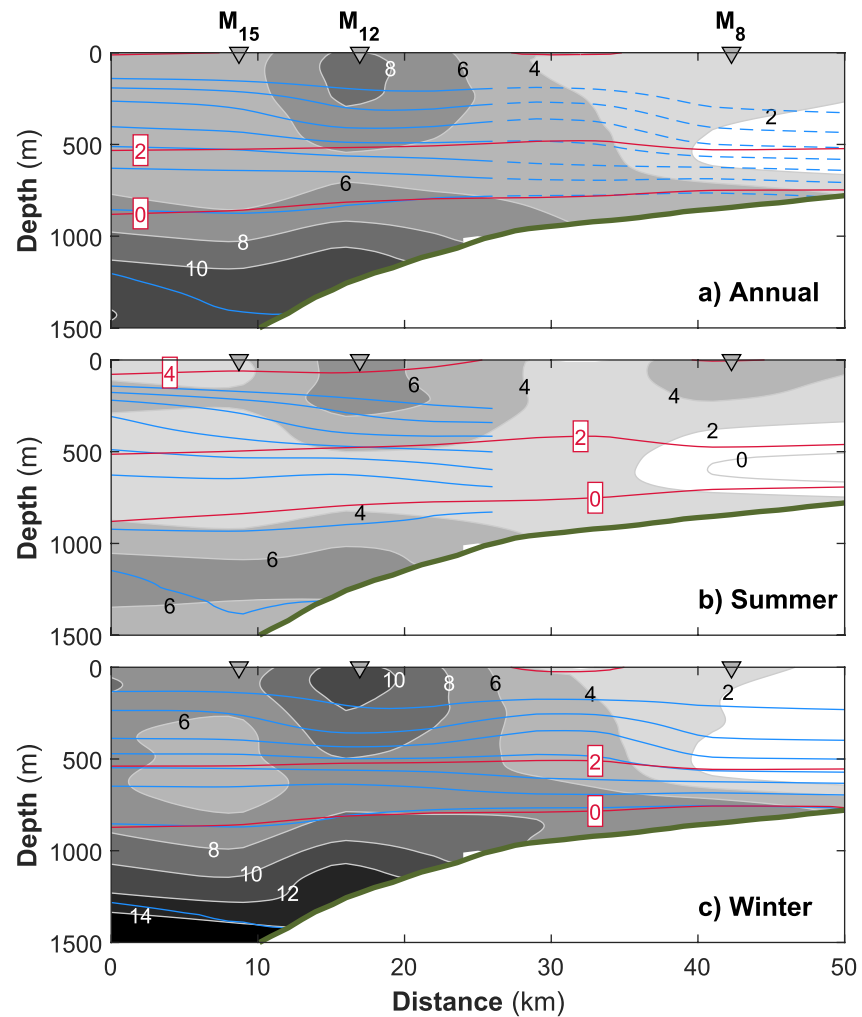


Figure 6. Mean sections of along-isobath current and hydrography from the daily fields interpolated using objective methods and averaged over (a) the entire record (annual), (b) summer months (JJA: June, July, August), and (c) winter months (DJF: December, January, February). Contours are for the along-isobath currents (filled gray scale, contours labeled at 2 cm s^{-1} intervals), potential density anomaly σ_0 (blue contours at 0.025 kg m^{-3} intervals, not labeled), and for the 0 , 2 and 4°C isotherms (red). The mooring locations are marked by triangles. Objective interpolation uses Gaussian correlation length scales of 20 km in the horizontal and 100 m in the vertical, and a 5% relative error (see text). While the current and temperature records are available for the entire record at M_8 , the instruments with conductivity sensors depleted their batteries by late May 2015 and the density contours in summer cannot be extended to M_8 . The annual average density contours at distances greater than 27 km (dashed lines) can therefore be biased and are averages from early September 2014 to late May 2015.

transport are highest from fall (October) through winter to March. When averaged over seasons, the transport in all temperature classes is stronger in winter and spring, except for $T > 3^\circ\text{C}$. In the AW, the largest transport occurs during winter in the $3\text{--}4^\circ\text{C}$ class. It is also noteworthy that there is substantial transport associated with waters colder than 0°C , exceeding 1 Sv annually, and reaching a maximum value close to 1.5 Sv in spring. The annual average AW transport is $1.1 \pm 0.2 \text{ Sv}$, with the maximum seasonal average in fall ($1.4 \pm 0.2 \text{ Sv}$, but winter is identical within error bars) and the minimum in summer ($0.8 \pm 0.1 \text{ Sv}$), see Table 3.

5. Energetics

We use a right-handed rotated coordinate system that is rotated 125° from East. In this system, x and y directed positively along-isobath and off-slope toward deeper water, respectively. The velocity components are along-isobath, u , and across-isobath, v . Fluctuations in the data are denoted by primes and are calculated by band-pass filtering the hourly data with cutoff frequencies corresponding to 14-day and 35-hr periods (see Section 3.3). Time aver-

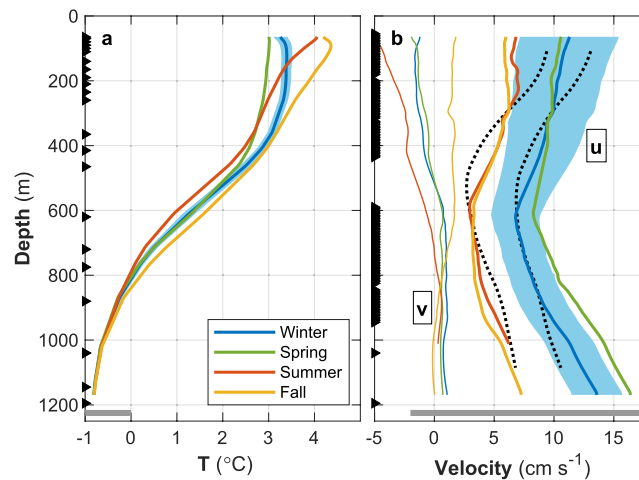


Figure 7. Mean profiles of (a) temperature and (b) velocity at M_{12} . Velocity profiles are shown for rotated components, along-isobath, u (positive toward northwest) and across-isobath, v (positive off slope toward deeper water). Additionally, the geostrophic velocity calculated from the winter and summer mean hydrographic profiles of M_{12} and M_{15} are shown (dotted black). The geostrophic velocity is referenced to direct measurements at 600 m. The target depths of sensors are marked on the left, and the gray horizontal lines indicate the seafloor depth. Time averaging is over winter (DJF), spring (MAM), summer (JJA) and fall (SON) months. The error envelope represents the standard error (degrees of freedom are 12, assuming a 7-day decorrelation time scale) and is shown for winter profiles only but is representative for all seasons.

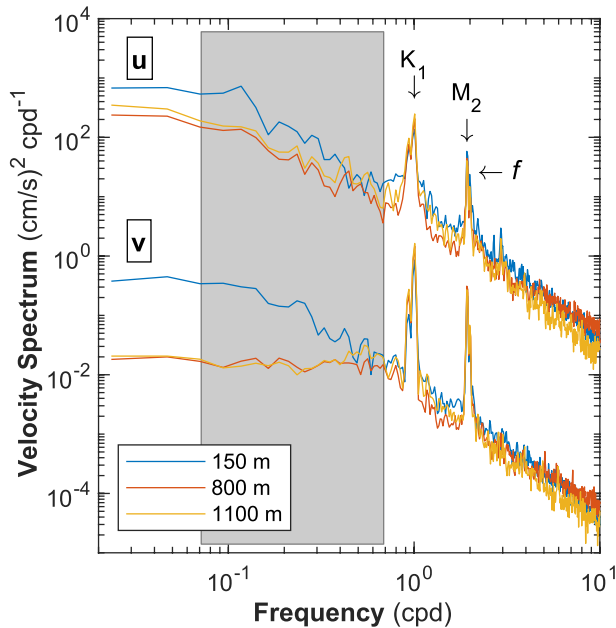


Figure 8. Frequency spectra of along-isobath, u , and across-isobath, v , velocity at M_{12} , at selected vertical levels in the upper ocean, at middepth, and close to the bottom. The spectra are obtained using the 1-hr, 5-m vertically gridded data time series, which is corrected for vertical mooring displacement and computed using half-overlapping 42.67 day segments (1,024 points). Each spectrum is an average of spectra calculated over 5 levels (25 m vertical range) centered at the indicated depth. The across-isobath spectra are shifted downward by a factor of 1,000 for clarity. The gray shading indicates the band-pass frequency range (14 days–35 hr period) used in eddy kinetic energy calculations, while the arrows indicate the main diurnal (K_1) and semidiurnal (M_2) tidal constituents, and the local inertial frequency, f , which is barely detected next to M_2 .

aging, denoted by an overbar, is performed over 30-day moving windows. The horizontal eddy kinetic energy (EKE) density is expressed in units of J kg^{-1} or $\text{m}^2 \text{s}^{-2}$ and is calculated as $\text{EKE} = 0.5(\overline{u'^2} + \overline{v'^2})$. The across-isobath component of kinematic eddy heat flux (EHF) is calculated as $\text{EHF} = \overline{v'T'}$.

The barotropic (BT) and baroclinic (BC) conversion rates are calculated using the formulations and the method identical to Fer et al. (2020), obtained by simplifying the conversion rates formulated for a 3D, right-handed coordinate system in Olbers et al. (2012, pp. 376–377):

$$\text{BT} = -\rho_0 \left(\overline{u'u' \frac{\partial \bar{u}}{\partial x}} + \overline{u'v' \left(\frac{\partial \bar{u}}{\partial y} + \frac{\partial \bar{v}}{\partial x} \right)} + \overline{v'v' \frac{\partial \bar{v}}{\partial y}} \right) \approx -\rho_0 \left(\overline{u'u' \frac{\partial \bar{u}}{\partial y}} \right), \quad (1)$$

and

$$\text{BC} = g \left(\frac{\partial \bar{\rho}}{\partial z} \right)^{-1} \left(\overline{u'\rho' \frac{\partial \bar{\rho}}{\partial x}} + \overline{v'\rho' \frac{\partial \bar{\rho}}{\partial y}} \right) \approx g \left(\frac{\partial \bar{\rho}}{\partial z} \right)^{-1} \left(\overline{v'\rho' \frac{\partial \bar{\rho}}{\partial y}} \right), \quad (2)$$

where ρ is the potential density referenced to the surface, g is the gravitational acceleration, and $\rho_0 = 1,027 \text{ kg m}^{-3}$ is a reference density. Equations 1 and 2 are approximations made under the assumption that there is no variability in the along-isobath direction and that the across-isobath gradients are dominant. This assumption is commonly used and considered acceptable when analyzing observations from a mooring array in a boundary current (see Fer et al. (2020) and references therein). A positive value of BT indicates that kinetic energy is transferred from the mean flow to eddies. This occurs as eddies transport along-isobath momentum down the mean velocity gradient, and is related to barotropic instability. A positive value of BC indicates conversion from the mean available potential energy into eddy potential energy. This occurs as eddies grow and extract energy from the mean state, and is related to baroclinic instability (Olbers et al., 2012). We estimate the mean vertical gradient used in calculating BT and BC from M_{12} , the mean

lateral gradients between M_{15} and M_{12} , and use the fluctuations measured at M_{12} (i.e., BC and BT are estimates at one mooring, M_{12}). Due to the limited density measurements available, we made calculations at 100 m intervals in the vertical between 100 and 1,100 m. At each 100-m level, we calculated properties as 20-m vertical averages using the 5-m vertical gridded fields over four levels. Note that there are no density measurements, and hence no BC estimates, at M_{12} after 11 May 2015, in the upper two levels (100 and 200 m).

Figure 11 shows profiles that have been averaged over the annual record length and different seasons. This temporal averaging takes into account many eddy time scales, typically 1 week, and is a good representation of the mesoscale energetics recorded by the mooring array. EKE and EHF are shown for each mooring, whereas BT and BC represent the conversion across M_{15} and M_{12} . In the shallow mooring, EKE in the upper 500 m is comparable to the deeper moorings only in winter and fall and is substantially less energetic in spring and summer. The EKE profiles in the deeper moorings are the largest and nearly identical in spring (with winter profiles being similar but slightly less energetic). Overall, the EKE decreases from the surface layer to quiescent levels below 500 m (see also Figure 9). At middepth, the annual-averaged EHF is positive, indicating that it is directed across-isobath toward deeper water, with a flux divergence from the middle to the outer mooring. The largest EHF is observed in winter at 600 m depth, where the average velocity profiles show a minimum (Figure 7).

The profiles of average conversion rate show distinct non-zero values, but they are generally inconclusive. This is discussed further in Section 6.3. The most notable BT conversion into EKE occurs in the upper 500 m during summer. However, during winter and spring, when EKE is stronger, BT exhibits conflicting signs of negative and positive, respectively. In contrast, BC opposes BT in winter and spring. Positive BC values during winter suggest that the enhanced EKE and the elevated middepth EHF may be supplied by baroclinic instability. Averaged over the upper 500 m, BC is negative (close to $3 \times 10^{-5} \text{ W m}^{-3}$) in fall and spring. The average BC value in winter and summer is about $1 \times 10^{-5} \text{ W m}^{-3}$. In general, the magnitude of seasonally averaged BC is larger than that of BT, with a 10-fold increase in fall and spring, and 4-fold increase in winter. The only exception is summer, when BC is only 50% larger. The signs of the average BT and BC are opposite in all seasons, except for summer.

Time series of EKE and conversion rates averaged vertically show their variability throughout the mooring record (Figure 12). The vertical averaging is carried out over the upper half of the water column (between 100 and

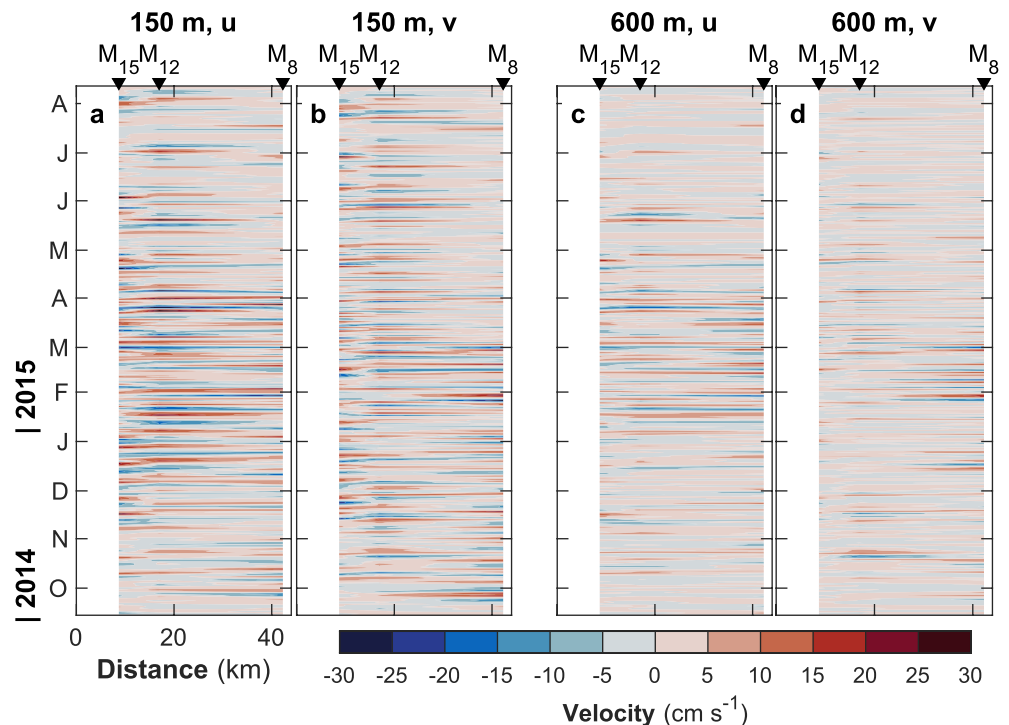


Figure 9. Hovmöller diagram of along-isobath, u , and across-isobath v velocity variability in the 14-day to 35-hr band, at (a and b) 150 m and (c and d) 600 m depth. Arrow heads mark the location of the three moorings.

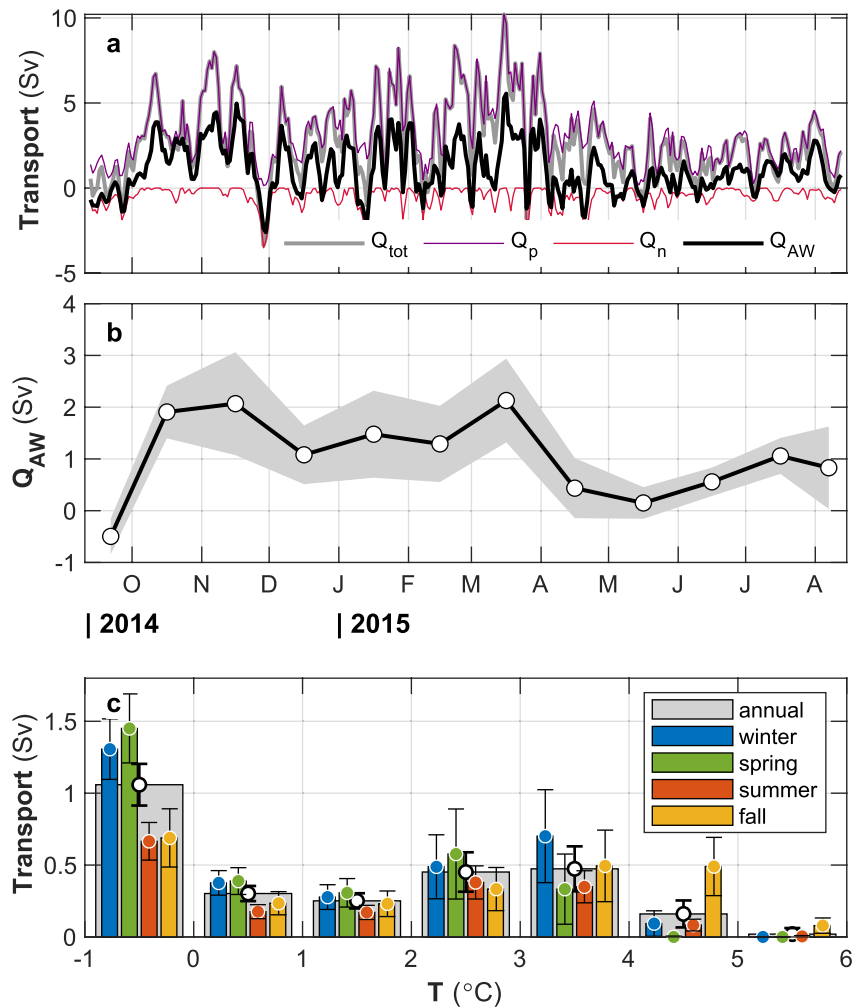


Figure 10. Transport estimates derived from the objectively interpolated daily fields at the mooring array. (a) Transport toward northwest out of the section (Q_p , positive; all temperature classes), toward southeast into the section (Q_n , negative, all temperature classes), total net transport $Q_{tot} = Q_p + Q_n$, and the net transport of the Atlantic Water, Q_{AW} , defined as water with temperature $T \geq 2^\circ\text{C}$. (b) Monthly averages of Q_{AW} with standard error envelope. (c) Net transport in temperature classes, averaged over the entire record (annual) and seasons. Error bars represent standard error, shown for the annual averages, winter, and fall.

500 m, above the velocity and EKE minimum) and the full depth (100–1,100 m). Additionally, Figure 12 presents the along- and across-isobath components of wind speed and depth-averaged currents (\mathbf{u}_{BT}) at M_{12} for reference. Lagged correlation analysis (not shown) does not indicate a definite relation between the local wind and \mathbf{u}_{BT} or EKE and conversion rates. From January to early April, the EKE is amplified by about a factor of two, with the highest EKE being recorded in March, following the peak in the depth-averaged u .

The layer-averaged conversion rates are generally weak, with BT typically ranging within $\pm 1 \times 10^{-5} \text{ W m}^{-3}$ and BC within $\pm 3 \times 10^{-5} \text{ W m}^{-3}$, except for two episodes in November and March when BC becomes negative and 2–5 times larger. Each event lasts about a week with peaks centered on 23 November 2014 and 8 March 2015, respectively. During these events, the temporal- and layer-averaged values between 100 and 500 m are approximately $-28 \times 10^{-5} \text{ W m}^{-3}$ and $-10 \times 10^{-5} \text{ W m}^{-3}$. Excluding these two periods, the temporal average BC is not significantly different from zero, but positive conversion rates of about $3 \times 10^{-5} \text{ W m}^{-3}$ occur in October and February. It should also be noted that the conversion rates at the M_{12} location may not be representative of the volume-averaged conversion rates over the slope (Section 6.3).

Table 3
Volume Transport Calculations

Period	n	Transport (Sv)		
		Q_p	Q_n	Q_{AW}
Summer	10	2.2 [± 0.3 ; ± 0.1]	-0.3 [± 0.1 ; ± 0.1]	0.8 [± 0.2 ; ± 0.1]
Fall	11	3.2 [± 0.6 ; ± 0.2]	-0.5 [± 0.2 ; ± 0.2]	1.4 [± 0.5 ; ± 0.2]
Winter	13	3.9 [± 0.5 ; ± 0.2]	-0.5 [± 0.2 ; ± 0.2]	1.3 [± 0.4 ; ± 0.2]
Spring	13	3.7 [± 0.6 ; ± 0.1]	-0.6 [± 0.2 ; ± 0.1]	0.9 [± 0.4 ; ± 0.1]
Annual	48	3.3 [± 0.3 ; ± 0.2]	-0.5 [± 0.1 ; ± 0.2]	1.1 [± 0.2 ; ± 0.2]

Note. Positive transport, Q_p is directed northwest out of the section, Q_n is southeastward, and Q_{AW} is the total AW transport with $T \geq 2^\circ\text{C}$. n is the degrees of freedom (the number of daily data points divided by the decorrelation time of 7 days). The values shown in square brackets are [\pm standard error; \pm total error]. The standard error is calculated as σ/\sqrt{n} , where σ is the standard deviation. The total error estimate is derived from the objective mapping and measurement errors (refer to the text for details).

6. Discussion

6.1. Transport and Its Variability

The transport estimates in our study can be compared to those reported in previous literature, which mainly used numerical models. For example, Athanase et al. (2021) used the $1/12^\circ$ Mercator Ocean operational physical system to estimate the AW transport over a 14-year period (2007–2020). They found that 45% of the modeled AW inflow in WSC recirculated toward Fram Strait. Using the sections reported in their study, we can compare our calculated transports by using 55% of the WSC transport and removing the Svalbard branch. This results in an average transport estimate of 1.6 Sv, with 2.2 and 1.1 Sv in January and July, respectively. These values are larger than our estimate of 1.1 Sv, but they agree with our observation of relatively larger transports in winter (1.3 Sv) compared to summer (0.8 Sv). However, it is important to note that the model used by Athanase et al. (2021) did not include tidal forcing and was not fully eddy-resolving, which could contribute to the discrepancy. Furthermore, Athanase et al. (2021) defined AW using a temperature threshold of 1°C . When we include the additional transport of 0.3 Sv from the $1\text{--}2^\circ\text{C}$ class to our estimates, the difference between our estimate and theirs reduces to our estimated transport error of ± 0.2 Sv.

Crews et al. (2019) used an 800-m horizontal resolution sea ice and ocean model for Fram Strait and the surrounding waters of Svalbard. The model used is the same as the one employed in Hattermann et al. (2016) and shown in Figure 2. The transport difference between the WSC and the combined transports of Yermak Pass and Svalbard branch can be directly comparable to our mooring array. According to their model that was analyzed over four years (July 2005 to July 2009), the AW transport across our array would be 1.6 Sv in winter and 0.7 Sv in summer. These values are in fairly good agreement with our observations of 1.3 ± 0.2 Sv and 0.8 ± 0.1 Sv, respectively. It should be noted that Crews et al. (2019) defined AW as having $T > 1.5^\circ\text{C}$ and $S > 34.85$. However, due to a 1°C cold bias in their model, our definition of the AW is similar.

To investigate the influence of wind stress variability on the Yermak branch transport, we calculated the lagged correlation coefficient between the wind stress curl field and the depth-averaged along-slope velocity at M_{12} . The correlation coefficients (Figure 13a) are significant within the 95% confidence interval on the southern YP, with a maximum observed along the northwestern coastline of Spitsbergen, over the pathway of the Svalbard branch. Thus, a positive wind stress curl on the southern YP, resulting in a divergence of surface water on the Plateau, leads to an increased volume transport in the Yermak branch. Conversely, a negative wind stress curl reduces the Yermak branch transport. Wind stress along a coastline produces similar effects. Since the Svalbard branch flows along the coast, we consider coastal upwelling with divergence of surface water along the coast, and downwelling resulting in convergence of surface water, to be the main driver of geostrophic flow anomalies in the Svalbard branch (Nilsen et al., 2021). Note that a southerly wind component close to the coastline, driving coastal downwelling, will create a negative wind stress curl on the YP, while a northerly wind component will set up a positive wind stress curl. Thus, while coastal upwelling associated with northerly wind, or downwelling with southerly wind, is the driving mechanism for the Svalbard branch, one may refer to the sign of wind stress curl as an indicator of its effect on the transport.

By compositing all wind stress curl fields for cases when the Yermak branch transport is larger than one standard deviation from the mean, an average wind stress field pattern emerges (Figure 13b) that supports a coastal upwelling along the northwestern coastline of Spitsbergen and a divergence of surface water. As shown in Nilsen et al. (2021), this reduces the northwestward transport of AW in the Svalbard branch across the YP. Thus, the significant correlation (Figure 13a) on the southern flanks indicates a switching mechanism between the Yermak and Svalbard branches. Northeasterly winds over the Plateau decrease the Svalbard branch transport, and more of the AW in the WSC is channeled to the Yermak branch, whereas southwesterly winds on the YP and in eastern Fram Strait (Figure 13b) increase the Svalbard branch transport. This switching mechanism is also evident in a comparison of transport estimates in Figures 10a and 10b with Figure 18 in Nilsen et al. (2021); the volume transport anomaly in the Svalbard branch is positive during December–January 2015, when the Yermak branch transport is reduced compared to the end of March when it reached its maximum and the Svalbard branch had a negative transport anomaly.

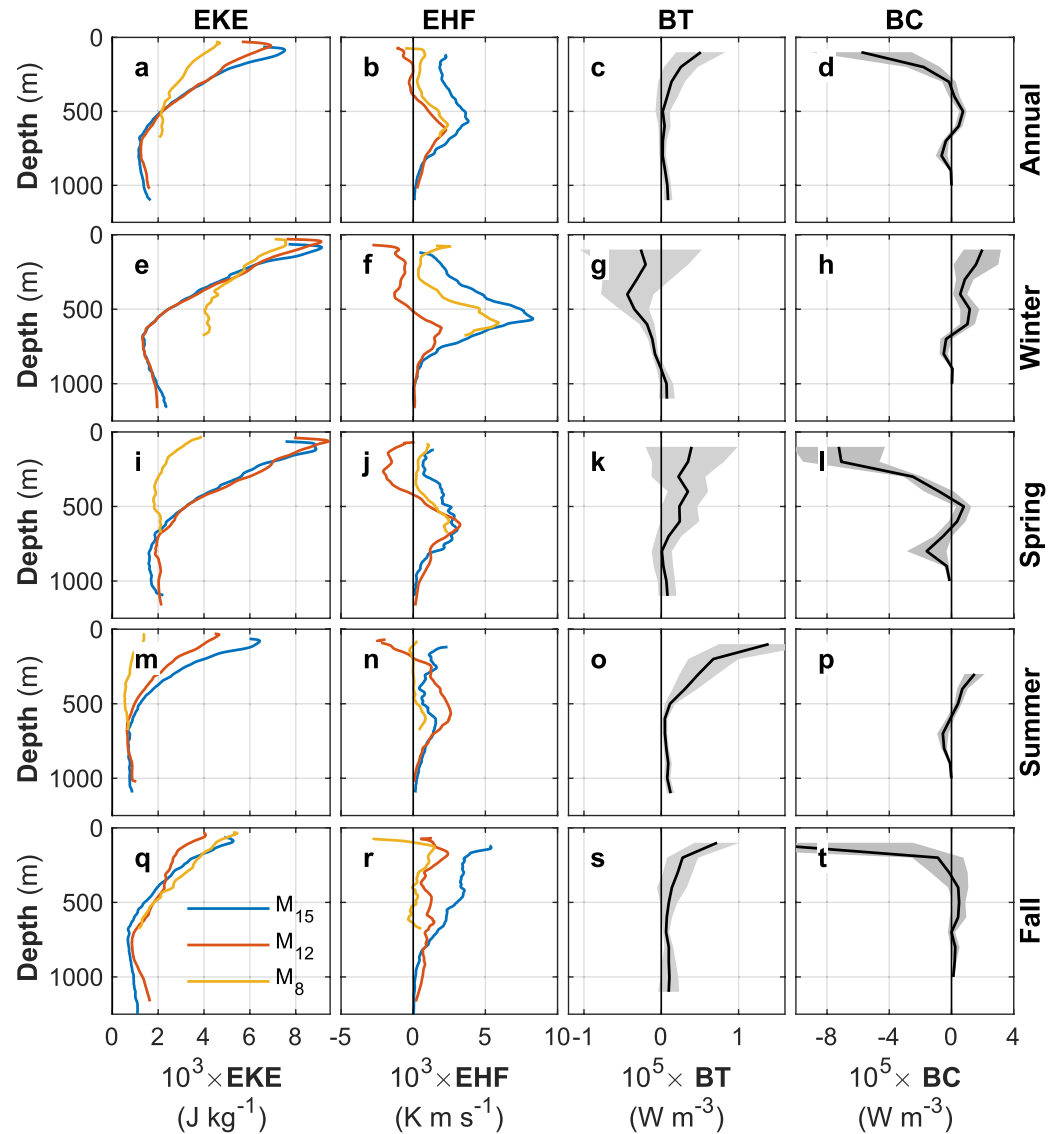


Figure 11. Profiles of horizontal eddy kinetic energy (EKE), kinematic eddy heat flux (EHF), barotropic conversion rate (BT), and baroclinic conversion rate (BC), displayed in columns. Each row represents time averages over different seasons including annual (the entire record, a–d), winter (e–h), spring (i–l), summer (m–p), and fall (q–t). The EKE and EHF profiles are shown for each mooring (colors). The conversion rates are calculated using data from M_{15} and M_{12} , as described in the text. Error bars indicate the standard error, calculated using a decorrelation time scale of 7 days. The off-scale value near the surface in panel (t) is -13.4×10^{-5} .

6.2. Cold, Deep Current

The deep, bottom-enhanced current of cold water is captured at the outer two moorings, M_{12} and M_{15} . Throughout the record, the layer-averaged current between 800 and 1,200 m is 30% larger at M_{12} , measuring 9 cm s^{-1} . The current is largest in spring, measuring 14 cm s^{-1} , compared to summer and fall (5 cm s^{-1}). The average vertical shear between the 800 and 1,200 m levels is approximately 1 cm s^{-1} per 100 m at both moorings, and weakest in summer, while it is largest in spring with approximately a factor of two. This shear is consistent with the geostrophic shear calculated from the horizontal density difference between M_{12} and M_{15} (Figure 7). This bottom-enhanced current has not been described in detail before, and its dynamical consequences on the transport of warm AW in the Yermak branch are not known. Our observations are too limited to investigate the dynamics of the cold, deep-boundary current.

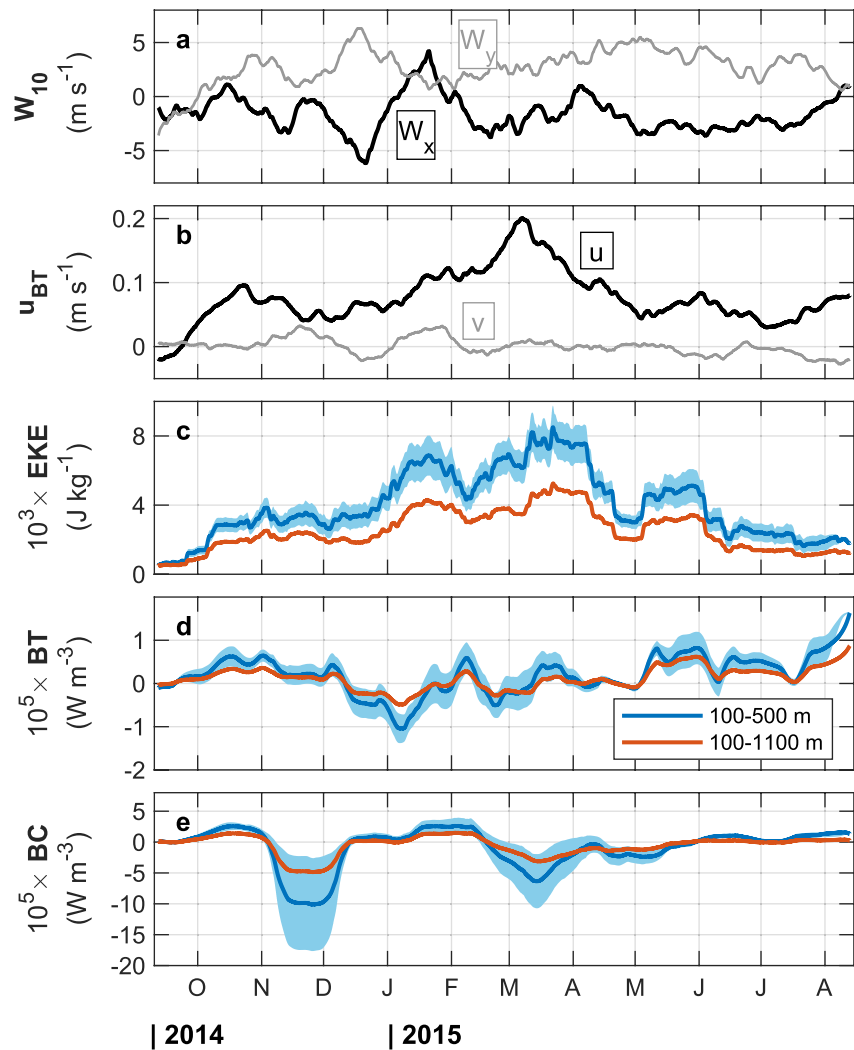


Figure 12. Time series of (a) wind speed rotated into along-isobath (W_x) and across-isobath (W_y) components (b) along-isobath (u) and across-isobath (v) depth-averaged velocity and (c) eddy kinetic energy (EKE) at M_{12} , (d) barotropic conversion rate (BT), and (e) baroclinic conversion rates (BC). EKE and the conversion rates are vertically averaged over 100–500 m and 100–1,100 m, with time averaging over 30-day moving windows. Error bars indicate the standard error using a decorrelation time scale of 7 days and shown only for the 100–500 m average with the largest variability.

The WSC offshore branch, as defined in Beszczynska-Möller et al. (2012) along the 78°50'N array, shows a bottom-intensified current with cold water ($<0^\circ\text{C}$) at approximately the 1,400 m isobath (their Figure 2). This branch is located to the west of the 1,000-m isobath. Long-term average volume transport estimates of the (total) WSC in temperature classes (as shown in their Figure 3) suggest a net northward volume transport of approximately 2 Sv, associated with “deep waters” colder than 0°C . Note that these estimates cover the WSC core on the shelf and upper slope, the offshore branch west of the 1,000-m isobath, as well as the outer recirculating WSC branch extending as far out as 1°W . In the recirculating WSC branch, the northward and southward contributions to the volume transport likely cancel out (see their Figure 2c), and the net transport of deep water is dominated by the bottom-enhanced core at the lower slope. We speculate that our observed deep cold current is an extension of this core and is therefore a coherent current with a volume transport of approximately 2 Sv. However, our outer mooring does not fully capture this current, resulting in an underestimation of the volume transport in our observations.

Ice formation in Svalbard polynyas produces dense, brine-enriched shelf waters that descend the continental slope as a dense water plume (Akimova et al., 2011; Fer & Ådlandsvik, 2008; Quadfasel et al., 1988). In some winters, with a sufficient increase in source water salinity on shelves, the plume sinks to depths deeper than

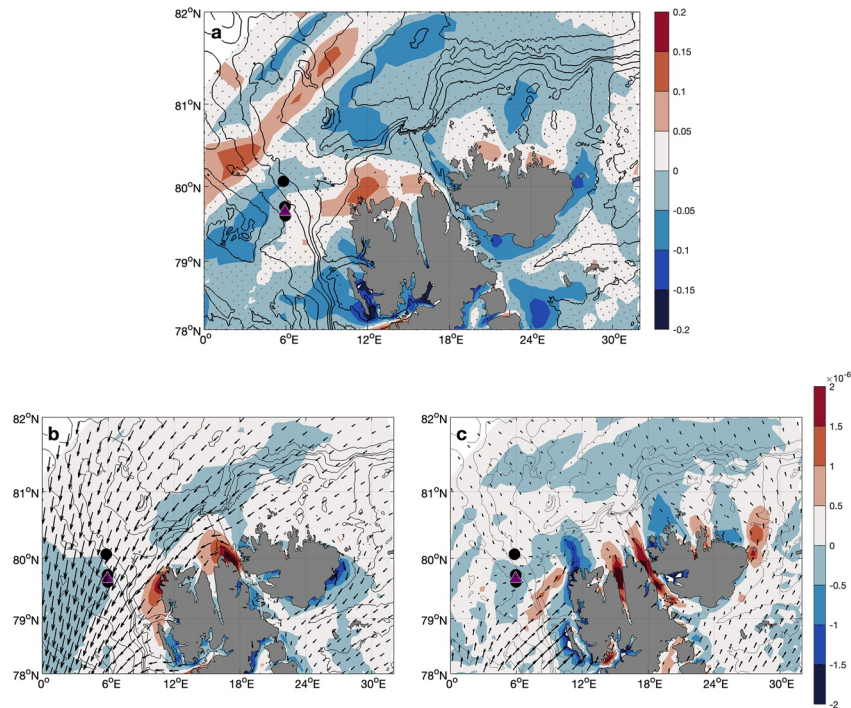


Figure 13. Correlation estimates (with zero lag) between NORA10 wind fields and mooring time series at M_{12} . (a) Correlation coefficients between the wind stress curl field and the depth-averaged along-slope velocity at M_{12} . The composite average surface wind stress (arrows) and wind stress curl field (color) for all cases when the depth-averaged along-slope velocity at M_{12} is (b) greater than one standard deviation and (c) less than negative one-standard deviation, corresponding to the largest directional variability in the along-slope velocity. Mooring locations south of the Yermak Plateau are marked with black dots, and the NORA10 grid point nearest to the mooring location (hourly wind vector at 10-m height used in Figure 4) is marked by a triangle. In (a), gray dots indicate areas that are not significant at the 95% confidence level.

1,000 m in Fram Strait. The bottom-intensified cold current observed in our moorings may be related to such a plume. However, deep plume observations in Fram Strait are rare: Akimova et al. (2011) detected the plume in Fram Strait only in three winters out of 20 years of observations. Moreover, at these latitudes, the plume spreads as a bottom current and is 30–80 m thick, much smaller than our observations where the cold current spans several hundred meters vertically at both the 1,500 m and 1,200 m isobaths. Another characteristic of the plume is the relatively increased near-bottom salinity. Observed salinity in deep Fram Strait, associated with the outflow plume, ranges from 34.92 to 34.97. During our observation period, salinity measurements at 15 m above the seabed at 1,040 m depth are available roughly 250 km upstream of our mooring site (Bensi et al., 2019). This record, closer to source regions and on the path of an eventual dense plume, does not show any anomalously high salinity throughout 2015, suggesting a lack of bottom plume during our observation period. At M_{15} , at 65 m above the seafloor, $S < 34.93$ at all times, and only less than 2% of the record shows $S > 34.92$. We conclude that the persistent deep flow of cold water we have observed is not associated with dense waters convected from the shelves.

6.3. Conversion Rates

Our calculations using the outer two moorings resulted in small barotropic and baroclinic conversion rates overall, with BT varying within $\pm 1 \times 10^{-5} \text{ W m}^{-3}$ and BC varying within $\pm 3 \times 10^{-5} \text{ W m}^{-3}$, except for two episodes with large negative BC events. Note, however, that the conversion rates are not quantified in other parts of the slope and can differ from those at the M_{12} location. In October and mid-January to mid-February, positive BC of $\approx 3 \times 10^{-5} \text{ W m}^{-3}$ could potentially generate EKE through baroclinic instability. Conversion through barotropic instability is at most one third of BC. The annual average of BT is $0.2 \times 10^{-5} \text{ W m}^{-3}$. When averaged over the upper 500 m, the average BC value in winter and summer is about $1 \times 10^{-5} \text{ W m}^{-3}$. Excluding the two events

with large negative BC, the annual average BC is not significantly different from zero. For reference, a conversion rate of 10^{-5} W m^{-3} for 1 day accounts for EKE of $10^{-3} \text{ J kg}^{-1}$, which is typically 4 to 8 times less than the observed EKE (Figure 12c). Given the relatively weak conversions, we do not investigate further the conditions for barotropic or baroclinic instability.

Wekerle et al. (2020) analyzed conversion rates from two eddy-resolving models with around 1 km mesh resolution in Fram Strait, covering the WSC and our mooring site. According to their results, energy transfer (BT and BC) mainly occurs along the pathway of the WSC core, approximately along the 500–1,000 m isobaths. BT energy conversion (between mean kinetic energy and EKE) is bidirectional, while BC energy conversion (between available potential energy and EKE) is mainly positive, revealing conversion to EKE. Typical depth-integrated kinematic conversion rates along the slope (500–1,000 m depth) are $(1 - 5) \times 10^{-5} \text{ m}^3 \text{ s}^{-3}$ (2006–2009 average, their Figure 12), which corresponds to a depth-averaged conversion rate of approximately $(1 - 5) \times 10^{-5} \text{ W m}^{-3}$ at a total depth of 1,000 m. The average BC conversion rate in our Yermak mooring site (80°N) is $(1 - 3) \times 10^{-5} \text{ W m}^{-3}$, and BT is weak and approximately zero in both models. These rates are similar to our observations.

Our estimates of conversion rates are relatively small compared to those of other observational studies conducted in major currents in high latitudes. For example, in the Norwegian Atlantic slope current in the Lofoten escarpment, the barotropic and baroclinic conversion rates (averaged over 14 and 3 months in summer, respectively) were approximately $(3 - 5) \times 10^{-5} \text{ W m}^{-3}$ (Fer et al., 2020). In the WSC (averaged over 12 years), BT was on the order of $1 \times 10^{-5} \text{ W m}^{-3}$, while BC was $5 \times 10^{-5} \text{ W m}^{-3}$ in summer at 75 m depth, increasing to $1.5 \times 10^{-4} \text{ W m}^{-3}$ in winter (von Appen et al., 2016). In the shelfbreak EGC (averaged over 11 months, excluding a reversal event), BT at 100 m was on the order of $1 \times 10^{-5} \text{ W m}^{-3}$ and BC varied in the range of $(1 - 5) \times 10^{-4} \text{ W m}^{-3}$ (Håvik et al., 2017). For comparison, the values of EKE in these studies were similar to our observations in the Yermak branch: in the Norwegian Atlantic slope current, the annual average EKE was $6.5 \times 10^{-3} \text{ J kg}^{-1}$, and $10 \times 10^{-3} \text{ J kg}^{-1}$ in winter; in the WSC, the EKE was $5 \times 10^{-3} \text{ J kg}^{-1}$ in summer $20 \times 10^{-3} \text{ J kg}^{-1}$ in winter at 75 m depth, and the magnitude was approximately halved at 250 m depth; in the shelfbreak EGC, the EKE was in the range of $(1-10) \times 10^{-3} \text{ J kg}^{-1}$ at 100 m. Although the conversion rates in our observations are significantly smaller than the annual averages in these other currents, shorter temporal averages are comparable, but on the smaller end. We note that a more favorable agreement can be obtained in the upper 250 m in our observations; however, we argue that sufficient volume averaging must be applied to obtain reliable estimates of conversion rates.

The EKE and conversion rates measured at M_{12} share similarities with those observed at the 78°50'N array, located approximately 110 km to the south. von Appen et al. (2016) analyzed 16 years of measurements from the moorings to quantify and describe the mesoscale fluctuations and mechanisms for their generation through instabilities of the WSC. Their reported conversion rates and EKE are summarized above with reference to the WSC. Winter conditions with strong currents and a greater vertical shear favor the baroclinic instability of the WSC, resulting in more eddies. In contrast, the current is relatively stable in summer, forming fewer eddies. The pattern of EKE and BC we observe is similar. While von Appen et al. (2016) suggest the eddies generated over the slope are likely advected westward and captured by their moorings in the central Fram Strait, northward advection of eddies toward our mooring site is also possible. Furthermore, average EKE maps determined from sea surface height anomalies measured by satellite-based altimeter show, in addition to high EKE near the 78°50'N array, another patch of high EKE about 50 km north. It is likely that this location, closer to our array, is a region of significant conversion rates and EKE generation that can be advected to our mooring locations. This can contribute to a relatively increased EKE in winter and spring when the local conversion rates are small (Figure 12).

The conversion rates calculated from our moorings may not accurately represent the volume-averaged conversion rates. A similar issue was discussed in Fer et al. (2020) regarding the Norwegian Atlantic slope current, where BT and BC estimated from a pair of moorings were compared to volume-averaged conversion rates from a high-resolution numerical model. The results showed that BT had a highly variable spatial structure, including a change in sign, which could not be resolved with a pair of moorings. Additionally, BC was not captured by the calculations from a single level. As a result, the authors concluded that the mooring-derived conversion rates must be interpreted with caution and may not be representative of the actual conversion rates in the region. Although our vertical coverage and averaging in the Yermak branch are better than that in Fer et al. (2020), inter-

preting the time series of BT and BC is complex. A better spatial averaging is needed to accurately quantify the conversion rates in this region.

In two episodic events, BC dominates the time series with significantly large negative values, indicating that eddies are transferring energy back to the mean flow. According to Wekerle et al. (2020), the negative conversion rates inferred from eddy-resolving models indicate areas where eddy fluxes interact with sloping topography, causing dense water to be lifted onto the continental shelf (Tverberg & Nøst, 2009). As a result, upward-sloping isopycnals near the seafloor increase the available potential energy of the mean field in those regions. We speculate that this process may have contributed to the negative conversion rates observed in our estimates.

7. Summary and Conclusions

We analyzed measurements from an array of three moorings deployed on the southwestern slope of the YP between 10 September 2014 and 13 August 2015. The array covers the AW boundary current along the slope, referred to as the Yermak branch—an important contributor of oceanic heat to the Arctic Ocean. Our observations allowed us to describe the structure and seasonal variability of the Yermak branch, mesoscale current variability and energy conversion rates, and estimate the volume transport. These are the first year-round moored measurements targeting the Yermak branch.

Temporal-averaged sections across the mooring array show a surface-intensified AW core captured by the middle mooring, which is strongest in winter but persists year-round at the core. Average currents in winter are twice as strong as those in summer and fall across the water column. Water above 500 m depth is always above 2°C across the section. At the core mooring, the along-isobath current is directed toward the Arctic Ocean and frequently reaches 40 cm s⁻¹. Beneath the surface-intensified core, the average velocity profile reduces to a subsurface minimum followed by a bottom-intensified cold current. The shape of the average velocity profiles is consistent with geostrophic shear. The cold, bottom-boundary current is in the same direction as the Yermak branch, visible in all seasons and strongest in winter and spring. It is likely that the deep cold current we observe is a coherent current, and an extension of the bottom-intensified current observed beneath the offshore branch of the WSC along the 78°50'N array.

The annual average AW transport is 1.1 ± 0.2 Sv with a maximum seasonal average in fall (1.4 ± 0.2 Sv), and a minimum in summer (0.8 ± 0.1 Sv). There is substantial transport associated with waters colder than 0°C, exceeding 1 Sv averaged annually and reaching a maximum value close to 1.5 Sv in spring. The dynamics of this cold boundary current and its potential impact on the Yermak branch need further studies.

The volume transport of the Yermak branch is regulated by the wind stress curl and coastal upwelling driving a divergence of surface water on the YP, leading to a switching between the Yermak and Svalbard branches of AW. The depth-averaged along-isobath velocity at the core, hence the Yermak branch transport, is significantly correlated with the wind stress curl field over the pathway of the Svalbard branch. A positive wind stress curl gives rise to an increased volume transport in the Yermak branch.

The mesoscale fluctuations share similarities with those observed at the 78°50'N array, located approximately 110 km to the south our array. The largest mesoscale (35-hr to 14-day band) variability is observed during winter. At middepth, the band-passed currents are substantially suppressed relative to the upper ocean, and the variability is mainly in winter and early spring. With the caveat of limited spatial coverage of the mooring array, we estimate the barotropic conversion rates (related to barotropic instability) and the baroclinic conversion rates (related to baroclinic instability). The average conversion rates are small and inconclusive. In the upper 500 m, the average baroclinic conversion during winter and summer is about 1×10^{-5} W m⁻³. The seasonally averaged baroclinic conversion is higher than the barotropic conversion, with about a ten-fold increase in fall and spring and a four-fold increase in winter. The most distinct barotropic conversion into EKE occurs in the upper 500 m during summer.

It is worth noting that the location of our mooring array is not ideal, and it may include some unquantified contributions to the Yermak Pass and recirculation branches. While our observations help to constrain the structure and variability of currents and AW volume transport, a mooring array specifically designed to capture the Yermak branch is needed. Ideally, it should cover the northern flank of YP near 81°N. Moreover, during the time

of our observations, the site was typically in open waters. The impacts of sea-ice cover, which can mediate the atmospheric forcing and modify the vertical structure of surface-intensified sheared geostrophic currents, will be important for the northern parts of the Yermak branch and merit further studies.

Data Availability Statement

The mooring data are openly available from <https://doi.org/10.21335/NMDC-1508183213> (Fer & Peterson, 2019). ROMS 800 m resolution ocean and sea ice circulation model data are accessible from <https://doi.org/10.21334/npolar.2017.2f52acd2> (Albretsen et al., 2017). EUMETSAT Ocean and Sea Ice Satellite Application Facility, Global SIC Near-Real-Time product, OSI-401-b, is available from http://doi.org/10.15770/EUM_SAF_OSI_NRT_2004 (OSI-SAF, 2017). NORA10 is a hindcast archive for Scandinavian areas produced at MET Norway (Reistad et al., 2011) and can be downloaded from <https://thredds.met.no/thredds/projects.html> upon requesting an account. In parts of our analyses and presentation of the data, we used the software packages from Lilly (2021) and Pawlowicz (2020).

References

- Aagaard, K., Foldvik, A., & Hillman, S. R. (1987). The West Spitsbergen Current: Disposition and water mass transformation. *Journal of Geophysical Research*, 92(C4), 3778–3784. <https://doi.org/10.1029/jc092ic04p03778>
- Akimova, A., Schauer, U., Danilov, S., & Núñez-Riboni, I. (2011). The role of the deep mixing in the Storfjorden shelf water plume. *Deep-Sea Research I*, 58(4), 403–414. <https://doi.org/10.1016/j.dsr.2011.02.001>
- Albretsen, J., Hattermann, T., & Sundfjord, A. (2017). Ocean and sea ice circulation model results from Svalbard area (ROMS) [Dataset]. Norwegian Polar Institute. <https://doi.org/10.21334/npolar.2017.2f52acd2>
- Artana, C., Provost, C., Koenig, Z., Athanase, M., & Asgari, A. (2022). Atlantic water inflow through the Yermak Pass branch: Evolution since 2007. *Journal of Geophysical Research*, 127(2), e2021JC018006. <https://doi.org/10.1029/2021JC018006>
- Athanase, M., Provost, C., Artana, C., Pérez-Hernández, M. D., Sennéchaël, N., Bertoso, C., et al. (2021). Changes in Atlantic water circulation patterns and volume transports north of Svalbard over the last 12 years (2008–2020). *Journal of Geophysical Research*, 126(1), e2020JC016825. <https://doi.org/10.1029/2020JC016825>
- Bensi, M., Kovacevic, V., Langone, L., Aliani, S., Ursella, L., Goszczko, I., et al. (2019). Deep flow variability offshore south-west Svalbard (Fram Strait). *Water*, 11(4), 683. <https://doi.org/10.3390/w11040683>
- Beszczynska-Möller, A., Fahrbach, E., Schauer, U., & Hansen, E. (2012). Variability in Atlantic water temperature and transport at the entrance to the Arctic Ocean, 1997–2010. *ICES Journal of Marine Science*, 69(5), 852–863. <https://doi.org/10.1093/icesjms/fss056>
- Bourke, R. H., Weigel, A. M., & Paquette, R. G. (1988). The westward turning branch of the West Spitsbergen Current. *Journal of Geophysical Research*, 93(C11), 14065–14077. <https://doi.org/10.1029/jc093ic11p14065>
- Crews, L., Sundfjord, A., & Hattermann, T. (2019). How the Yermak pass branch regulates Atlantic water inflow to the Arctic Ocean. *Journal of Geophysical Research*, 124(1), 267–280. <https://doi.org/10.1029/2018JC014476>
- Dörr, J., Árhun, M., Eldevik, T., & Madonna, E. (2021). Mechanisms of regional winter sea-ice variability in a warming Arctic. *Journal of Climate*, 34(21), 8635–8653. <https://doi.org/10.1175/jcli-d-21-0149.1>
- Fer, I., & Ádlandsvik, B. (2008). Descent and mixing of the overflow plume from Storfjord in Svalbard: An idealized numerical model study. *Ocean Science*, 4(2), 115–132. <https://doi.org/10.5194/os-4-115-2008>
- Fer, I., Bosse, A., & Dugstad, J. (2020). Norwegian Atlantic slope current along the Lofoten Escarpment. *Ocean Science*, 16(3), 685–701. <https://doi.org/10.5194/os-16-685-2020>
- Fer, I., & Peterson, A. K. (2019). Moored measurements of ocean current, temperature and salinity from Yermak Plateau, September 2014–August 2015 [Dataset]. Norwegian Marine Data Centre. <https://doi.org/10.21335/NMDC-1508183213>
- Gascard, J. C., Richez, C., & Roault, C. (1995). New insights on large-scale oceanography in Fram Strait: The West Spitsbergen Current. In W. O. Smith Jr. & J. Grebmeier (Eds.), *Arctic oceanography, marginal ice zones and continental shelves* (Vol. 49, pp. 131–182). AGU.
- Hattermann, T., Isachsen, P. E., von Appen, W.-J., Albretsen, J., & Sundfjord, A. (2016). Eddy-driven recirculation of Atlantic water in Fram Strait. *Geophysical Research Letters*, 43(7), 3406–3414. <https://doi.org/10.1002/2016GL068323>
- Håvik, L., Våge, K., Pickart, R. S., Harden, B., Appen, W.-J. V., Jonsson, S., & Østerhus, S. (2017). Structure and variability of the shelfbreak East Greenland Current North of Denmark Strait. *Journal of Physical Oceanography*, 47(10), 2631–2646. <https://doi.org/10.1175/jpo-d-17-0062.1>
- Hofmann, Z., von Appen, W.-J., & Wekerle, C. (2021). Seasonal and mesoscale variability of the two Atlantic Water recirculation pathways in Fram Strait. *Journal of Geophysical Research*, 126(7), e2020JC017057. <https://doi.org/10.1029/2020JC017057>
- Ingvaldsen, R. B., Assmann, K. M., Primicerio, R., Fosheim, M., Polyakov, I. V., & Dolgov, A. V. (2021). Physical manifestations and ecological implications of Arctic Atlantification. *Nature Reviews Earth & Environment*, 2(12), 874–889. <https://doi.org/10.1038/s43017-021-00228-x>
- Koenig, Z., Provost, C., Sennéchaël, N., Garric, G., & Gascard, J.-C. (2017). The Yermak Pass Branch: A major pathway for the Atlantic water north of Svalbard? *Journal of Geophysical Research*, 122(12), 9332–9349. <https://doi.org/10.1002/2017JC013271>
- Large, W. G., & Pond, S. (1981). Open ocean momentum flux measurements in moderate to strong Winds. *Journal of Physical Oceanography*, 11(3), 324–336. [https://doi.org/10.1175/1520-0485\(1981\)011<0324:OOMFMI>2.0.CO;2](https://doi.org/10.1175/1520-0485(1981)011<0324:OOMFMI>2.0.CO;2)
- Leng, H., Spall, M. A., & Bai, X. (2022). Temporal evolution of a geostrophic current under sea ice: Analytical and numerical solutions. *Journal of Physical Oceanography*, 52(6), 1191–1204. <https://doi.org/10.1175/jpo-d-21-0242.1>
- Lilly, J. M. (2021). jLab: A data analysis package for Matlab, v.1.7.1 [Software]. Zenodo. <https://doi.org/10.5281/zenodo.4547006>
- Manley, T. O. (1995). Branching of Atlantic water within the Greenland-Spitsbergen passage: An estimate of recirculation. *Journal of Geophysical Research*, 100(C10), 20627–20634. <https://doi.org/10.1029/95jc01251>
- Nilsen, F., Ersdal, E. A., & Skogseth, R. (2021). Wind-driven variability in the Spitsbergen Polar Current and the Svalbard branch across the Yermak Plateau. *Journal of Geophysical Research*, 126(9), e2020JC016734. <https://doi.org/10.1029/2020JC016734>

- NOAA National Geophysical Data Center. (2006). *2-minute Gridded Global Relief Data (ETOPO2)* v2. NOAA National Centers for Environmental Information. <https://doi.org/10.7289/V5J1012Q>
- Olbers, D., Willebrand, J., & Eden, C. (2012). *Ocean dynamics*. Springer Verlag Berlin.
- Orvik, K. A., & Niiler, P. (2002). Major pathways of Atlantic water in the northern North Atlantic and Nordic Seas toward Arctic. *Geophysical Research Letters*, *29*(19), 2-1–2-4. <https://doi.org/10.1029/2002GL015002>
- OSI-SAF. (2017). Global Sea Ice Concentration (netCDF) - DMSF, EUMETSAT SAF on Ocean and Sea Ice. https://doi.org/10.15770/EUM_SAF_OSI_NRT_2004
- Padman, L., Plueddemann, A. J., Muench, R. D., & Pinkel, R. (1992). Diurnal tides near the Yermak Plateau. *Journal of Geophysical Research*, *97*(C8), 12639–12652. <https://doi.org/10.1029/92jc01097>
- Pawlowicz, R. (2020). M_Map: A mapping package for MATLAB, version 1.4 m [Software]. M_Map. www.eoas.ubc.ca/~rich/map.html
- Peterson, A. K. (2017). *Mixing processes in the changing Arctic Ocean* (Ph.D. thesis). University of Bergen.
- Peterson, A. K., & Fer, I. (2017). *Measurements of ocean currents, temperature and salinity from moorings at the Yermak Plateau: September 2014–September 2015 (Technical Report)*. Geophysical Institute, University of Bergen.
- Polyakov, I. V., Pnyushkov, A. V., Alkire, M. B., Ashik, I. M., Baumann, T. M., Carmack, E. C., et al. (2017). Greater role for Atlantic inflows on sea-ice loss in the Eurasian Basin of the Arctic Ocean. *Science*, *356*(6335), 285–291. <https://doi.org/10.1126/science.aai8204>
- Quadfasel, D., Gascard, J. C., & Koltermann, K. P. (1987). Large-scale oceanography in Fram Strait during the 1984 marginal ice-zone experiment. *Journal of Geophysical Research*, *92*(C7), 6719–6728. <https://doi.org/10.1029/jc092ic07p06719>
- Quadfasel, D., Rudels, B., & Kurz, K. (1988). Outflow of dense water from a Svalbard fjord into the Fram Strait. *Deep-Sea Research*, *35*(7), 1143–1150. [https://doi.org/10.1016/0198-0149\(88\)90006-4](https://doi.org/10.1016/0198-0149(88)90006-4)
- Reistad, M., Breivik, O., Haakenstad, H., Aarnes, O. J., Furevik, B. R., & Bidlot, J.-R. (2011). A high-resolution hindcast of wind and waves for the North Sea, the Norwegian Sea, and the Barents Sea. *Journal of Geophysical Research*, *116*(C5), C05019. <https://doi.org/10.1029/2010JC006402>
- Schauer, U., Fahrbach, E., Østerhus, S., & Rohardt, G. (2004). Arctic warming through the Fram Strait: Oceanic heat transport from 3 years of measurements. *Journal of Geophysical Research*, *109*(C6), C06026. <https://doi.org/10.1029/2003JC001823>
- Tverberg, V., & Nøst, O. A. (2009). Eddy overturning across a shelf edge front: Kongsfjorden, west Spitsbergen. *Journal of Geophysical Research*, *114*(C4), C04024. <https://doi.org/10.1029/2008JC005106>
- Uppala, S. M., Kållberg, P. W., Simmons, A. J., Andrae, U., Bechtold, V. D. C., Fiorino, M., et al. (2005). The ERA-40 re-analysis. *Quarterly Journal of the Royal Meteorological Society*, *131*(612), 2961–3012. <https://doi.org/10.1256/qj.04.176>
- von Appen, W.-J., Schauer, U., Hattermann, T., & Beszczynska-Möller, A. (2016). Seasonal cycle of mesoscale instability of the West Spitsbergen Current. *Journal of Physical Oceanography*, *46*(4), 1231–1254. <https://doi.org/10.1175/jpo-d-15-0184.1>
- Walczowski, W., Piechura, J., Osinski, R., & Wiczorek, P. (2005). The West Spitsbergen Current volume and heat transport from synoptic observations in summer. *Deep-Sea Research I*, *52*(8), 1374–1391. <https://doi.org/10.1016/j.dsr.2005.03.009>
- Wang, S., Cao, A., Li, Q., & Chen, X. (2022). Diurnal and semidiurnal internal waves on the southern slope of the Yermak Plateau. *Scientific Reports*, *12*(1), 11682. <https://doi.org/10.1038/s41598-022-15662-0>
- Wekerle, C., Hattermann, T., Wang, Q., Crews, L., von Appen, W. J., & Danilov, S. (2020). Properties and dynamics of mesoscale eddies in Fram Strait from a comparison between two high-resolution ocean-sea ice models. *Ocean Science*, *16*(5), 1225–1246. <https://doi.org/10.5194/os-16-1225-2020>